Structure of Oxalate Decarboxylase from *Bacillus subtilis* at 1.75 Å Resolution[†,‡]

Ruchi Anand, Pieter C. Dorrestein, Cynthia Kinsland, Tadhg P. Begley,* and Steven E. Ealick*

Department of Chemistry and Chemical Biology, Cornell University, Ithaca, New York 14853

Received February 1, 2002; Revised Manuscript Received April 18, 2002

ABSTRACT: Oxalate decarboxylase is a manganese-dependent enzyme that catalyzes the conversion of oxalate to formate and carbon dioxide. We have determined the structure of oxalate decarboxylase from *Bacillus subtilis* at 1.75 Å resolution in the presence of formate. The structure reveals a hexamer with 32-point symmetry in which each monomer belongs to the cupin family of proteins. Oxalate decarboxylase is further classified as a bicupin because it contains two cupin folds, possibly resulting from gene duplication. Each oxalate decarboxylase cupin domain contains one manganese binding site. Each of the oxalate decarboxylase domains is structurally similar to oxalate oxidase, which catalyzes the manganese-dependent oxidative decarboxylation of oxalate to carbon dioxide and hydrogen peroxide. Amino acid side chains in the two metal binding sites of oxalate decarboxylase and the metal binding site of oxalate oxidase are very similar. Four maganese binding residues (three histidines and one glutamate) are conserved as well as a number of hydrophobic residues. The most notable difference is the presence of Glu333 in the metal binding site of the second cupin domain of oxalate decarboxylase. We postulate that this domain is responsible for the decarboxylase activity and that Glu333 serves as a proton donor in the production of formate. Mutation of Glu333 to alanine reduces the catalytic activity by a factor of 25. The function of the other domain in oxalate decarboxylase is not yet known.

Oxalic acid is implicated in a wide range of environmental and biological processes, largely as a major chelator of metal ions such as Ca^{2+}, Al^{3+}, and Mn^{2+}. Oxalate chelates manganese from soil and thus stimulates an extracellular glycosylated manganese-dependent peroxidase involved in lignin degradation (*1*). Secretion of oxalic acid by fungi is associated with pathogenesis in plants such as bean, tomato, and sunflower (*2*), possibly by acting synergistically with pectolytic enzymes. Oxalate may also chelate calcium pectate of the host cell wall resulting in maceration. Accumulation of oxalate in leafy plants such as spinach and *Amaranthaceae* causes nutritional stress, as these plants lack the ability to catabolize oxalate (*3*). Humans and other vertebrates lack enzymes that act on oxalic acid and rely on intestinal bacteria to catabolize oxalic acid occurring from dietary sources. Consumption of leafy vegetables in humans may cause hyperoxaluria (*4*) in which precipitation of calcium oxalate leads to kidney stones. This problem can also occur in farm ruminants such as sheep and goats resulting in aversion to fodder with high oxalate content (*5*).

Oxalic acid production in microorganisms and fungi is associated with enzymes that degrade oxaloacetate and glyoxylate. Oxalic acid is also a byproduct of the degradation of L-ascorbic acid in some plants and fungi (*6*, *7*). Oxalate is catabolized in three major ways: by oxidation, by decarboxylation of oxalyl-coenzyme A, and by direct decarboxylation. Oxalate oxidases catalyze the conversion of oxalate to CO_2 and H_2O_2 in certain plants such as barley (*8*). Oxalate oxidase, also known as germin, and a related group of germin-like proteins are produced in plants in response to fungal pathogens and to abiotic stress. Oxalate is the main carbon source for *Oxalobacter formigenes*, which colonizes in the gastrointestinal tracts of vertebrates (*9*). *O. formigenes* catabolizes oxalic acid through the cyclic action of two enzymes. First, formyl-CoA transferase activates oxalate to oxalyl-CoA while releasing formate and then oxalyl-CoA decarboxylase, a thiamine pyrophosphate-dependent decarboxylase, converts oxalyl-CoA back to formyl-CoA and CO_2 (*10*).

Direct decarboxylation of oxalate to formate and CO_2 is catalyzed by oxalate decarboxylase (OXDC).[1] The best characterized OXDCs are from fungi, such as white-rot wood decaying *Flammulina velupties* (*3*) and *Aspergillus niger* (*11*). Recently, the *yvrK* gene from *Bacillus subtilis* was shown to encode an OXDC (*12*). The *yoaN* gene from *B. subtilis* may also encode an OXDC based on high sequence similarity with the known OXDCs (*13*). OXDC acts exclusively on oxalate and does not require any organic cofactor to catalyze the decarboxylation reaction. Instead, OXDCs are metalloenzymes and require manganese for function. The

[†] This work was supported by National Institutes of Health Grant DK44083 (to T.P.B.) and Biomedical Research Resource Program Grant RR01646. S.E.E. is indebted to the W. M. Keck Foundation and the Lucille P. Markey Charitable Trust.

[‡] The Brookhaven Protein Data Bank code for oxalate decarboxylase is 1J58 and for the oxalate decarboxylase complex with formate is 1L3J.

* To whom correspondence should be addressed at the Department of Chemistry and Chemical Biology, Cornell University, Ithaca, NY 14850. Telephone: (607) 255-7961. Fax: (607) 255-1227. E-mail: see3@cornell.edu or tpb2@cornell.edu.

[1] Abbreviations: OXDC, oxalate decarboxylase; OXO, oxalate oxidase; IPNS, isopencillin *N*-synthase; PMI, phosphomannose isomerase; P3H, proline 3-hydroxylase; HGDO, homogentisate dioxygenase; AraC, arabinose binding protein; βME, β-mercaptoethanol; SeMet, selenomethionine; CoA, co-enzyme A; CHESS, Cornell High Energy Synchrotron Source; DM, density modification; FOM, figure of merit; RMSD, root-mean-square deviation.

10.1021/bi0200965 CCC: $22.00
Published on Web 05/23/2002

activity of OXDC is also reported to show oxygen dependence (*13*). Oxalate decarboxylases have been used in the clinical assay of oxalate in blood and urine (*14*). Introducing an oxalate decarboxylase gene into plants that lack the ability to catabolize oxalate may be advantageous as it might relieve nutritional stress in crop plants and confer resistance to certain fungi (*2*).

The fungal OXDCs are induced by oxalate and are thought to control excess oxalate concentrations, while the *B. subtilis* OXDC is not oxalate induced, but acid induced (*12*). All of the known OXDCs are acidic and exhibit maximal activity at low pH. The isoelectric point of the *B. subtilis* enzyme was determined experimentally to be 6.1, higher than the predicted value of 5.1 (*12*). The pH−activity profile shows a bell-shaped curve with 70% activity at pH 3.0, maximal activity at pH 5.0, and no activity at pH 7.5 (*12*). Recent kinetic studies on *B. subtilis* OXDC reported a K_m of 15 mM and k_{cat} of 54 s^{-1}. Compared to the values reported for the fungal enzymes, K_m for the *B. subtilis* enzyme is about an order of magnitude higher while the value of k_{cat} is about 3-fold lower (*13*).

OXDC from *B. subtilis* is a 264 kDa homohexameric enzyme. OXDCs were predicted to belong to the cupin (from the Latin cupa, meaning small barrel) superfamily of proteins (*13*). The cupin family of proteins is defined by a characteristic β-sandwich domain having one six-stranded β-sheet and one five-stranded β-sheet (*2*, *15*). The cupin fold was first observed in the three-dimensional structures of the seed storage proteins phaseolin (*16*, *17*) and canavalin (*18*, *19*). Like OXDC, these proteins are classified as bicupins because each monomer has two β-barrel domains. The cupin fold has also been identified in the structures of isopencillin *N*-synthase (*20*), phosphomannose isomerase (*21*), the transcription factor AraC (*22*), dTDP-4-dehydrorhamnose 3,5-epimerase (*23*), homogentisate dioxygenase (*24*), oxalate oxidase (*25*), proline 3-hydroxylase (*26*), and the seed storage protein proglycinin (*27*). Many other proteins, transcription factors, and enzymes have been predicted on the basis of sequence to belong to the cupin superfamily (*2*, *15*, *28*).

In this work, we describe the three-dimensional crystal structure of *B. subtilis* OXDC at 1.75 Å resolution and compare its structure to other proteins with cupin folds. We also propose a mechanism that explains how OXDC catalyzes a difficult decarboxylation reaction using manganese.

MATERIALS AND METHODS

Expression and Purification of Native OXDC. Genomic DNA from *B. subtilis* CU1065 was used as a template for the PCR amplification of *yvrK* using 5′-AGG AGG AAA CAT ATG AAA AAA CAA AAT GAC ATT CCG-3′ (inserts an *Nde*I site at the start codon) and 5′-CTT GCA GAG CTC GAG TGC TCT CTG CAA GCG GCA AGT C-3′ (inserts an *Xho*I site after the stop codon) as the primer pair. The *B. subtilis yvrK* gene was amplified using the polymerase chain reaction and cloned into the expression vector pET-16b [Novagen Inc.], which adds an N-terminal His_{10} tag to the protein with a factor Xa cleavage site. The expression construct was subsequently transformed into *Escherichia coli* B834 (DE3) cells [Novagen Inc.], which are auxotrophic for methionine. One liter of LB medium and 50 μg/mL of ampicillin was inoculated with 1 mL of saturated starter culture and incubated at 37 °C. When the culture reached an OD_{600} of approximately 0.6, the cells were induced with 200 μM isopropyl-β-D- thiogalactopyranoside for 5 h at 30 °C. Cells were harvested by centrifugation and resuspended in 30 mL of ice cold binding buffer (10 mM imidazole, 50 mM NaH_2PO_4, 500 mM NaCl, pH 8.0). All subsequent protein purification steps were carried out at 4 °C or on ice. Cells were lysed by two passes through a French press at 15 000 psi. Cell debris was removed by high-speed centrifugation. The clarified cell extract was mixed with a 3-mL slurry of Ni-nitrilotriacetic acid resin [Qiagen], which was prequilibrated in binding buffer, and gently stirred for 1 h. The resin was centrifuged for 10 min at slow speed, and the supernatant was decanted. The resin was resuspended in wash buffer (30 mM imidazole, 50 mM NaH_2PO_4, 500 mM NaCl, pH 8.0) and poured onto a nickel column. The column was washed with wash buffer until the $OD_{280} < 0.005$. The His-tagged oxalate decarboxylate was eluted with 300 mM imidazole, 50 mM NaH_2PO_4, 500 mM NaCl, pH 8.0. The eluted protein was dialyzed against 50 mM Tris, 300 mM NaCl, 2 mM βME, pH 7.9. The protein was concentrated to 3 mg/mL as determined using the Bradford assay (*29*) with bovine serum albumin as a standard. Purity was verified by running a 12% polyacrylamide gel followed by Coomassie staining (data not shown).

Expression and Purification of SeMet-OXDC. Production of SeMet-OXDC follows the same protocol as above with a few modifications. The cells were grown in 1 L cultures containing M9 medium supplemented with 40 μg/mL L-amino acids (not including methionine), 1× BME vitamin solution (GibcoBRL), 0.4%(w/v) glucose, 2 mM $MgSO_4$, 25 μg/mL $FeSO_4 \cdot 7H_2O$, 50 μg/mL ampicillin, 0.1 mM $CaCl_2$, and 40 μg/mL L-selenomethionine. This medium was inoculated with cells from a 1 mL saturated starter culture containing the above medium with L-methionine in place of L-selenomethionine to promote growth. The 5 mL starter cells were then pelleted and washed in the induction culture so as to remove all traces of L-methionine before inoculation into 1 L media. SeMet-OXDC was purified in the presence of 5 mM βME to protect against oxidation.

Crystallization of OXDC. Initial crystallization conditions for native His_{10} tagged OXDC were determined using the sparse matrix screens, Crystal Screen 1 and Crystal Screen 2 (Hampton Research) using 3 mg/mL of the above purified protein. Several conditions yielded crystals of varying quality. The optimized conditions were found to be 6% (w/w) PEG4000 and 200 mM Tris, pH 8.0. The crystals were grown at room temperature using the hanging-drop vapor diffusion technique. Drops (4 μL) containing 1:1 mixture of protein and reservoir solutions were optimal for crystal growth. Diffraction quality crystals grew over a period of 4−7 days. Under these conditions, OXDC crystallizes in the rhombohedral space group *R*32 with unit cell dimensions in the hexagonal setting of $a = 154.7$ Å and $c = 123.7$ Å. Each asymmetric unit contains one monomer corresponding to a calculated solvent content of 60%. Crystals of OXDC were also grown under the conditions described above except that 10 mM formate was added to the solution.

Data Collection and Processing. A four-wavelength MAD data set was collected on a single frozen SeMet-OXDC crystal on the F2 beamLine at the Cornell High Energy Synchrotron Source (CHESS). A cryoprotectant solution of

Table 1: Summary of Data Collection and Processing Statistics[a]

	Se MAD (CHESS F2)				CHESS F1
	edge	peak	remote	reference	complex
wavelength (Å)	0.9794	0.9791	0.9640	0.9807	0.930
resolution (Å)	2.0	2.0	2.0	1.75	1.9
no. of refls	311,227	310,930	313,861	406,760	386,839
no. of unique refl	38,381	38,381	38,378	57,307	44,192
redundancy	8.1	8.1	8.2	7.1	8.7
completeness	100 (99.6)	100 (99.7)	100 (100)	99.9 (99.7)	99.9 (99.9)
R_{sym} (%)[b]	6.1 (13.2)	6.6 (14.1)	6.2 (13.8)	8.3 (32.5)	8.8 (26.5)
I/σ	9.8 (5.3)	9.0 (4.9)	9.2 (4.0)	7.0 (2.3)	7.1 (3.1)

[a] Values for the outer resolution shell are given in parentheses: MAD F2 data, 2.11−2.00 Å for edge, peak, and remote; 1.84−1.75 Å for reference. CHESS F1 native OXDC−formate complex data, 2.00−1.90 Å. [b] $R_{sym} = \sum\sum_i|I_i - \langle I\rangle|/\sum\langle I\rangle$, where $\langle I\rangle$ is the mean intensity of the N reflections with intensities I_i and common indices h, k, l.

20% glycerol in the mother liquor was used to prevent damage during freezing. An X-ray absorption spectrum in the vicinity of the Se K-absorption edge was determined for the SeMet-OXDC crystal by recording X-ray fluorescence as a function of wavelength. Diffraction data were then collected to 1.75 Å resolution at wavelengths corresponding to the inflection point of the spectrum (0.9793 Å), the peak of the spectrum (0.9791 Å), a high energy remote (0.9640 Å) and a low energy remote (0.9807 Å). The data were measured in 1° oscillations with 10 s exposure times using a Quantum-4 CCD detector (San Diego Area Detector Systems) with a crystal to detector distance of 160 mm. To minimize systematic errors, Bijovet pairs at the different wavelengths were acquired close in time by collecting the data in 5° wedges followed by a wedge having inverse beam geometry (ϕ + 180°). A total of 90° of data were collected for each wavelength. The data were processed with MOSFLM (*30*) and scaled using SCALA (*31*). Data for the OXDC/formate complex were measured on CHESS station F1 and processed and scaled as described for the MAD data. Final data processing statistics are shown in Table 1.

MAD Phasing. The selenium atom positions were determined using direct methods as implemented in the Shake-and-Bake procedure of Hauptman and co-workers (*32*). The DREAR (*33*) suite of programs was used to calculate the normalized anomalous differences (ΔE) to 2.5 Å resolution, which were then input into the computer program SnB (*34*). A total of 1000 random trials were used with the 800 largest E values and 8000 triple phase relationships. For each trial, phases were refined for 150 cycles. The results of the 1000 trials showed a bimodal distribution of the minimal function and indicated that 84 of the random trials had resulted in solutions. All eight Se atom positions (excluding the N-terminal SeMet residue) were located.

The Se atom positions were refined, and phases were calculated to 2.0 Å resolution using the program MLPHARE (*35*) yielding experimental phases with an overall figure of merit (FOM) of 0.54. The phases were improved to a final FOM of 0.89 using solvent flattening and histogram matching as implemented in the computer program DM from CCP4 (*36*). The resulting map was readily interpretable and showed all of the secondary structural elements.

Model Building and Refinement. The Cα trace was built through clear stretches of electron density at 2.0 Å resolution using the computer program O (*37*) followed by addition of side chains. The eight SeMet residues, along with several aromatic residues and well-defined isoleucine residues, served as markers and aided in sequence alignment. The first eight residues, the last seven residues, a loop containing residues 161−164 and the N-terminal poly-His tag were not visible in the electron density map. The poorly defined 161−164 loop was eventually modeled using coordinates from the OXDC/formate complex (see below), which provided a reasonable fit to the broken electron density in that region. After refinement, the B-factors for the loop were similar to other regions of the protein, and the $2F_o - F_c$ Fourier map showed strong electron density.

Refinement of the initial model was carried out using the CNS (*38*) suite of programs. Several rounds of simulated annealing, conjugate gradient minimization using CNS followed by manual map refitting in O were performed. The phases were then extended from 2.0 to 1.75 Å resolution. At this point, electron density near the manganese ion of domain I was modeled as a formate molecule. Water molecules were included in subsequent rounds of refinement based on the criteria that the peak in difference electron density maps was greater than 3σ, and the water molecule formed at least one hydrogen bond with a protein, ligand, or solvent atom. The final data refinement statistics are presented in Table 2.

The structure of the OXDC/formate complex was determined at 1.9 Å resolution starting with the refined OXDC model. During refinement, a strong peak in the electron density map at the protein surface was modeled as a metal ion. The metal ion was included in the refinement as magnesium on the basis of peak height and refined B-factor. Additional electron density near the unknown metal was modeled as a second formate molecule. Refinement of the OXDC/formate complex structure was performed using a similar minimization and fitting cycle as described above for the unliganded OXDC structure.

Site-Directed Mutagenesis. Site-directed mutagenesis of *yvrK* was performed with the QuikChange Site-Directed Mutagenesis kit from Stratagene (La Jolla, CA). Several clones for each mutant were selected and sequenced and clones that had the correct mutation and no other sequence changes were selected and used for all further studies.

Assay for OXDC Activity (Formate). Enzyme (100 μg of mutant or wild type) was added to 15 mM oxalate in 50 mM citrate-phosphate buffer pH 4.0 in a volume of 5 mL. At various time intervals, 0.5 mL aliquots were removed, quenched with 0.8 mL of K_2HPO_4, pH 9.5, and 0.25 mL of a 45 mM NAD solution was added. After the sample was mixed thoroughly, 1 unit of formate dehydrogenase was

Table 2: Final Refinement Statistics

	Se-Met OXDC	OXDC−formate complex
resolution (Å)	25−1.75	2.5−1.9
total no. of non-hydrogen atoms	3218	3183
no. of protein atoms	2774	2774
no. of water atoms	441	403
no. of ligand atoms	3	6
no. of reflections in refinement	57039	44155
no. of reflections in test set	4063	4437
R factor (%)[a]	18.31	17.1
R_{free} (%)[b]	19.84	19.4
rms deviation from ideal geometry		
bonds (Å)	0.005	0.006
angles (deg)	1.3	1.5
Ramachandran plot		
most favored region (%)	87.5	88.1
additional allowed region (%)	11.2	10.6
generously allowed region (%)	0.0	0.0
disallowed region (%)	1.2	1.2
average B factors (Å^2)		
mainchain	12.4	11.9
side chain	14.6	15.1
water	24.2	28.0
formate	12.0	14.3
manganese ions	7.2	9.1
unknown metal ion[c]	12.1	12.5

[a] R factor $= \sum_{hkl}||F_{obs}| - k|F_{cal}|/\sum_{hkl}|F_{obs}|$, where F_{obs} and F_{cal} are observed and calculated structure factors, respectively. [b] R_{free} applies to a subset of reflections (10%) that were excluded from all stages of refinement. [c] For the purposes of refinement, the metal was designated as magnesium.

added, the reaction mixture was incubated at 37 °C for 20 min, and the absorbance at 340 nm ($\epsilon = 6220$ M^{-1} cm^{-1}) was recorded.

Assay for OXDC Activity (Carbon Dioxide). A 200 μL pipet tip was sealed on the narrow end using a Bunsen-burner, cut to fit into a 1.5-mL eppendorf tube, and loaded with 50 μL of 20% KOH. This together with 100 μL of 2.5 mM oxalate (600 000 cpm) in 200 mM NaPi-citrate pH 4.5 and 100 μg of protein from crude extract were added to a 1.5-mL eppendorf tube. The tube was closed immediately, incubated for the specified time at room temperature, quenched by the addition of 100 μL of 5 M H_2SO_4, and reclosed immediately. After 30 min, 50 μL of the KOH solution in the pipet tip was transferred to 1 mL of EtOH in a scintillation vial, 5 mL of scintillation fluid were added, and the liberated carbon dioxide was measured by scintillation counting.

OXDC is a difficult protein to work with. It is unstable and loses activity during purification, shows substrate inhibition, and undergoes partial precipitation during assays. This stability problem needs to be solved before a full kinetic characterization of the enzyme can be carried out.

RESULTS

Protein Architecture and Topology. The final model of OXDC contains residues 8−379 (Figure 1A). The structure of the OXDC monomer shows two cupin domains (Figure 1B). Domain I of OXDC comprises a continuous stretch of amino acid residues from 56 to 233. Domain II comprises residues 234−379 plus residues 8−55, which contribute one β-strand of the second cupin barrel and two short helices (Figure 1C). Each domain is characterized by one five-stranded antiparallel β-sheet and one seven-stranded antiparallel β-sheet. The two β-sheets form a jelly roll β-sandwich with a topology that is characteristic of the cupin barrel fold (*2*). Each of the 12 β-strands in the barrel is approximately perpendicular to the barrel axis. The two cupin domains of the monomer are linked by a pair of crossovers between the edge strands of the seven-stranded β-sheets. Several α-helices are attached to each domain, forming claw-like protrusions from the barrel that are involved in subunit contacts. Two α-helices at the N-terminus are also involved in subunit contacts. A manganese ion is located in the center of the cupin barrel of each domain. The manganese binding site is associated with a β-bulge in strand β5 of domain I and strand β17 of domain II.

Quaternary Structure of OXDC. The overall structure of OXDC is a hexamer made up of two trimeric layers packed face to face and having 32 (D_3) point symmetry (Figure 2). The diameter of the hexamer is approximately 90 Å, and the thickness is approximately 85 Å. A large solvent channel extends entirely through the hexamer along the 3-fold axis. The channel has a minimum dimension of about 15 Å near the center of the hexamer. The trimeric layers of the hexamer are stabilized by the interlocking claw-like α-helical protrusions of adjacent monomers (Figure 1). The claw of domain I from one monomer (helices α3 and α4) interlocks with the claw from domain II of an adjacent monomer (helices α5, α6, and α7). The two trimeric layers are joined through interactions of the N-terminal flanking regions (helices α1 and α2) of each monomer with the β-sheet domain (β1, β2, β4, and β20) of the molecule directly below. This interface contains several hydrogen bonds as well as hydrophobic contacts between residues along the edges of the β-barrel and the N-terminal α-helices.

Metal Binding Site. Each OXDC domain has a manganese-binding site that is buried deep inside the β-barrel (Figure 1B). The two manganese sites within the OXDC monomer are separated by approximately 26 Å. The manganese ion in each of the domains has an octahedral geometry in which four manganese ligands are contributed by highly conserved amino acid side chains (Figure 3). The manganese binding residues in domain I are His95, His97, His140, and Glu101 and in domain II are His273, His275, His319, and Glu280. In domain I, the remaining manganese sites are occupied by a water molecule and a formate molecule, and in domain II both of the remaining sites are occupied by water molecules. Interestingly, the formate molecule of domain I was present whether the enzyme was crystallized in the presence or absence of formate. The metal−atom coordination distances are in the range of 1.95 to 2.32 Å, consistent with the usual distances for manganese binding ligands (*39*).

The second shells of residues around the manganese ions are similar in both domains and are predominantly hydrophobic. The only hydrophilic residues in the second shell are Arg92 in domain I and Arg270 and Glu333 in domain II. The Nϵ atom of Arg92 in domain I faces away from the metal binding center and is hydrogen bonded to Asn167. In domain II, Arg270 hydrogen bonds with the oxygen atoms of Asp322 and Tyr340, which is near the entrance to the metal binding cavity. Glu333 is near the manganese binding site of domain II but makes no specific contacts with the metal or nearby residues. The corresponding residue in domain I is Leu153.

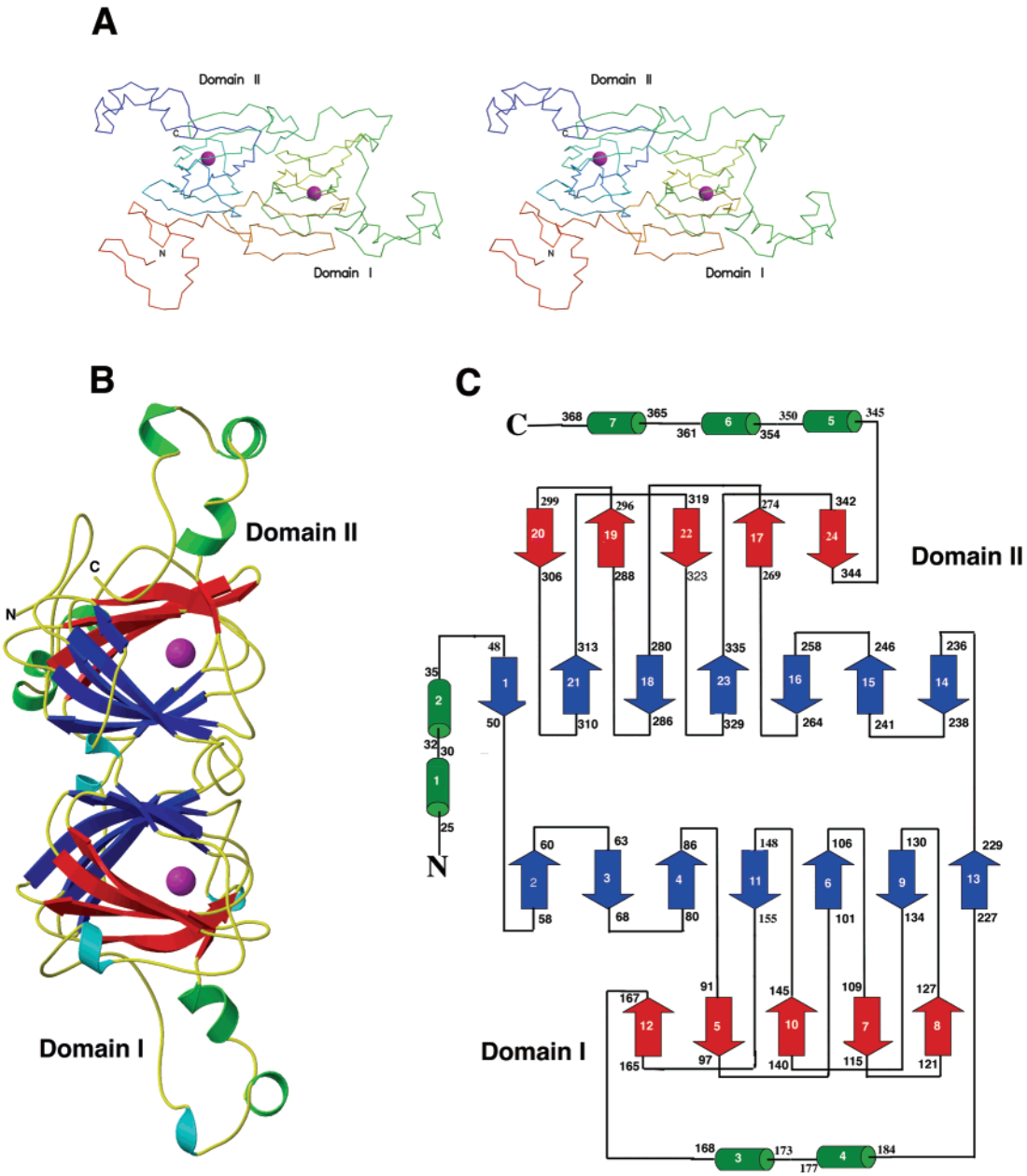

FIGURE 1: Structure of the OXDC monomer. (A) Stereoview of the Cα trace of OXDC. The coloring scheme is rainbow, changing from red to blue as the chain progresses from the N-terminus to the C-terminus. (B) Structure of the monomer of OXDC, highlighting the secondary structural elements, with β-sheets and α-helices colored as in panel C, 3_{10}-helices in cyan and loops in yellow. (C) Topology diagram of OXDC, showing the two domains I and II. The six-stranded β-sheets that make up the front of the cupin barrel are in blue, and the five-stranded β-sheets that make up the back are in red. The α-helices are shown in green. The first and last residue numbers of each secondary structural element are shown. The figure was prepared using MOLSCRIPT (*43*, *44*) and RASTER3D (*45*, *46*).

OXDC/Formate Complex. Two formate molecules were modeled in crystals of OXDC that were crystallized in solutions containing formate. One of the formate molecules is bound to the manganese ion of domain I, while the other is located near the surface of the hexamer. The B-factors of the manganese bound formate molecules were similar in both structures. One oxygen atom of the formate is coordinated to the manganese ion with an average distance of 2.18 Å for the two structures. The other oxygen atom is hydrogen bonded to the Nϵ atom of Arg92. This oxygen atom also forms a hydrogen bonding contact with the water molecule that completes the manganese coordination sphere. This water molecule in turn hydrogen bonds to Tyr200, which is an outlier in the Ramachandran plot.

The second formate site was observed only when formate was added during crystallization. This formate site is also located near a large peak in the electron density that we have interpreted as an unknown metal ion. This metal site is located near the surface of the hexamer and at the interface between two subunits, about 5 Å from the 2-fold axis. The density and temperature factor seem reasonable for the second row alkali metals with Mg^{2+} providing the best fit to the data. The metal binding site is in a hydrophilic cavity that contains a number of charged residues. The closest contact to the metal is His174 with a distance of 2.16 Å. His42 from the adjacent subunit also comes in close contact with the metal ion. The side chain of His42 is present in two conformations; one in which it makes contact with the

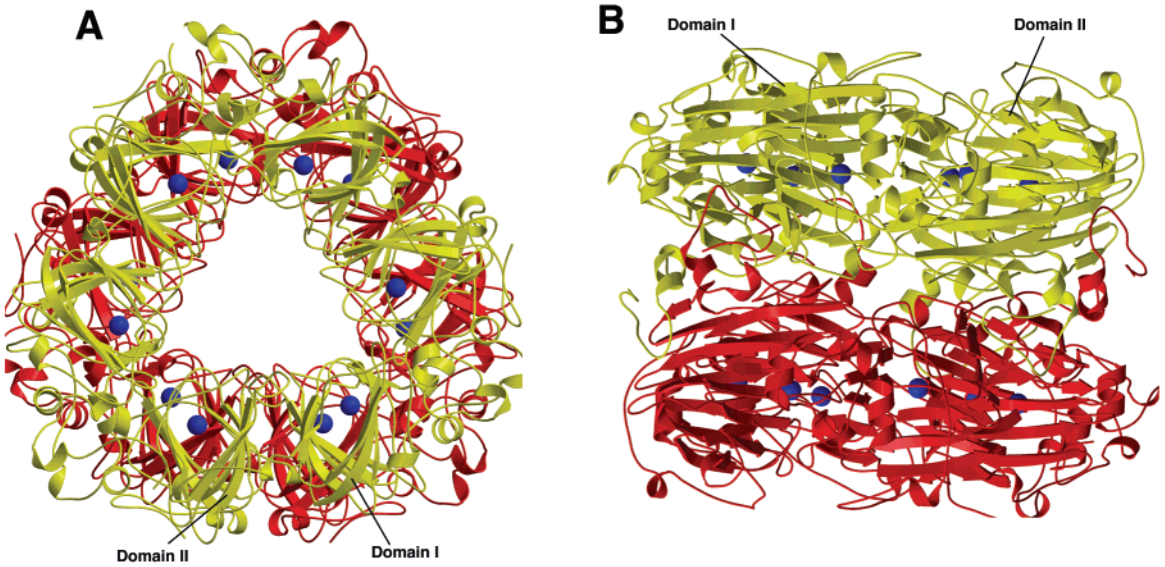

FIGURE 2: Structure of the OXDC hexamer. (A) View along crystallographic 3-fold axis. (B) View along crystallographic 2-fold axis with the 3-fold axis vertical. The figure was prepared using MOLSCRIPT (*43*, *44*) and RASTER3D (*45*, *46*).

Table 3: Summary of the Proteins with Known Structures Containing Cupin Folds

protein	fold	quaternary structure	metal (domain I/II)	ref
oxalate decarboxylase	bicupin	hexamer	Mn/Mn	this work
phaseolin	bicupin	trimer	none/none	(*16*, *17*)
canavalin	bicupin	trimer	none/none	(*18*, *19*)
proglycinin	bicupin	trimer	none/none	(*27*)
phosphomannose isomerase	bicupin	monomer	Zn/none	(*21*)
oxalate oxidase	monocupin	hexamer	Mn	(*8*)
homogentisate dioxygenase	monocupin[a]	hexamer	Fe[b]	(*24*)
proline 3-hydroxylase	monocupin	dimer	Fe	(*26*)
RmLC (epimerase)	monocupin	dimer	none	(*23*)
regulatory protein AraC	monocupin	dimer	none	(*22*)
isopenicillin *N*-synthase	monocupin	monomer	Fe[c]	(*20*)

[a] The structure contains a second domain that resembles a partially formed cupin barrel. [b] The Fe in this structure is not associated with the cupin domain. [c] The metal present in the crystal structure was Mn.

metal and the other in which it points away from the metal. The coordination geometry of the metal is roughly tetrahedral with the two histidine residues, formate, and a water molecule making up the coordination sphere (Figure 3C).

Activity of OxDc Mutants. The activities of native and mutant enzymes, determined using the formate and CO_2 release assays are shown in Figure 4. Formate production by the E333A mutant was reduced 25-fold compared to wild-type OXDC. CO_2 production for the E333A, the Y340F, and the R270E mutants was reduced by 4-, 13-, and 20-fold, respectively.

DISCUSSION

Comparison of OXDC with Other Protein Structures. OXDC is one of about a dozen structural examples of the cupin family. The common feature of this family is a β-sandwich with a jelly roll topology that resembles a barrel in which the strands run perpendicular to the barrel axis (*2*). The cupin family displays diverse biochemical functions and quaternary structures. In some instances, the monomeric unit consists of two independent cupin folds that are linked together to form bicupins. Many cupins contain metal binding sites, usually a first row transition metal. OXDC is the first structural example of a bicupin with two metal binding sites. OXDC is also the first example of a hexameric bicupin, having a total of 12 cupin domains with one manganese binding site each.

A database search using DALI (*40*) identified three seed storage proteins, a transcription factor, and six enzymes with structural homology to OXDC (Table 3). The three proteins phaseolin (*16*, *17*), canavalin (*18*, *19*), and proglycinin (*27*) are all classified as seed storage proteins. These seed storage proteins are trimeric bicupins with no metal binding sites but share some features of quaternary structure with the hexameric bicupin OXDC. Because the seed storage proteins lack metal binding sites, they also lack the metal binding residues that are often associated with the cupin fold. As with OXDC, the bicupin monomer of the seed storage proteins shows two crossovers between the two cupin domains: one after the first β-strand and one near the middle of the sequence. The seed storage proteins contain a long α-helix just before the second crossover that in OXDC corresponds to a loop with an extended structure. Overall, the trimer of the seed storage proteins is very similar to one of the trimeric layers within the OXDC hexamer. Like OXDC, the seed storage proteins utilize interlocking claw-like helical structures to form the trimer. The seed storage proteins lack the N-terminal helical overhang, which in OXDC is utilized in hexamer formation.

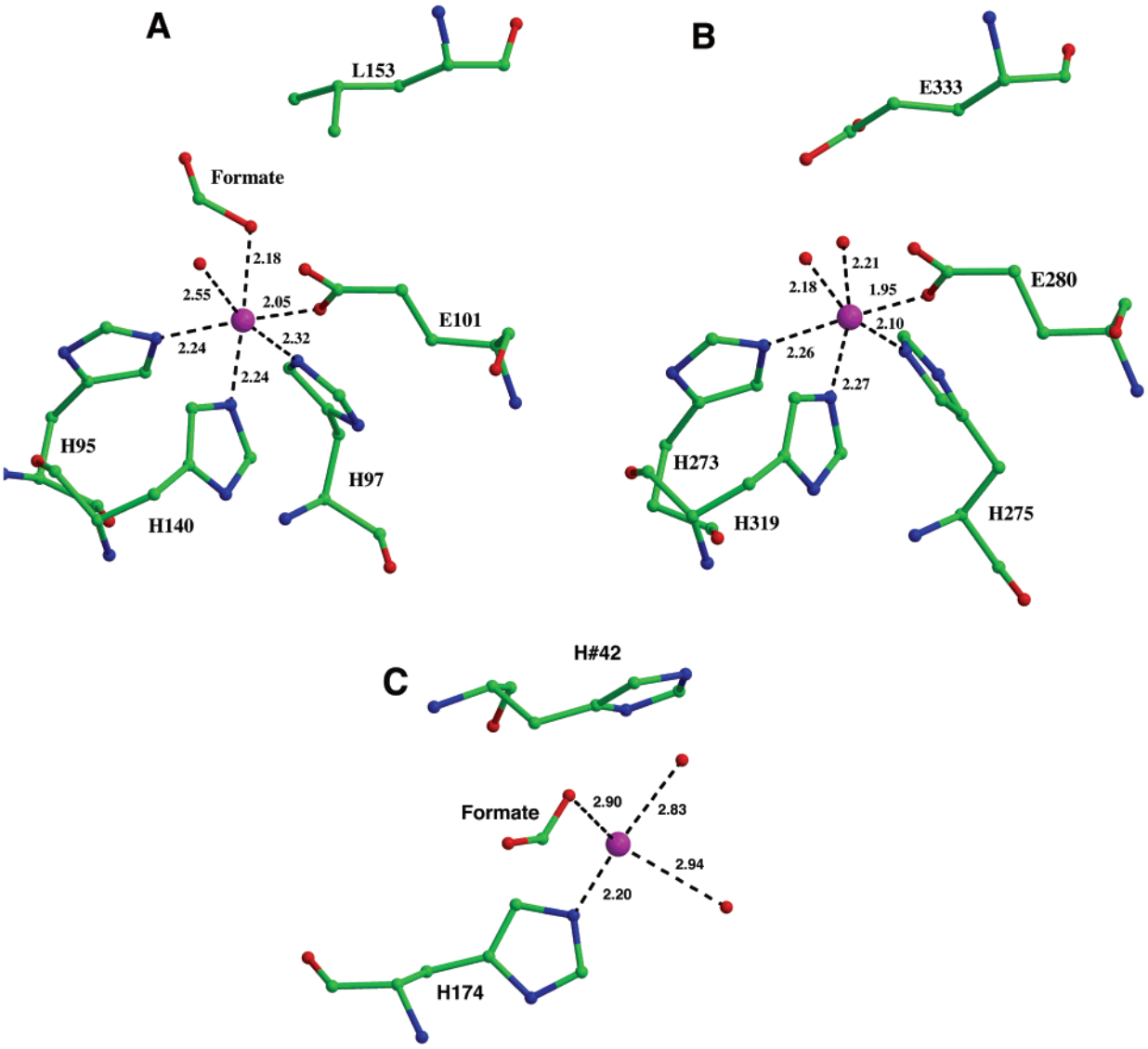

FIGURE 3: Comparison of metal binding sites of OXDC. (A) Manganese binding site of domain I. (B) Manganese binding site of domain II. (C) Unknown metal site at the protein surface. The metal was assigned as magnesium for the purposes of the X-ray refinement. The figure was prepared using MOLSCRIPT (*43*, *44*) and RASTER3D (*45*, *46*).

The enzymes with cupin folds have diverse functions. Most cupin enzymes are metalloenzymes in which the metals bind at similar locations with respect to the barrel. Phosphomannose isomerase (PMI) is a monomeric bicupin in which cupin domain I binds zinc while cupin domain II has no metal binding site (*21*). PMI has a large α-helical domain inserted between two β-strands from the five-stranded β-sheet of cupin domain I. In addition to the expected similarity of individual cupin domains, the two cupin domains of PMI are joined similarly as those of OXDC and the seed storage proteins. Specifically, the N-terminal β-strand begins domain II then crosses over to fully trace out domain I after which the polypeptide crosses back again to complete domain II. As PMI is monomeric, it lacks the helical protrusions of OXDC, which are utilized for formation of the hexamer. The zinc binding site of PMI is located deep in the β-barrel cavity of domain I. The zinc binding ligands consist of two histidines, a glutamate, and a glutamine. These residues correspond geometrically to the metal binding residues of OXDC. Unlike OXDC, in which the second shell of the manganese site is predominantly hydrophobic, the second shell of the PMI zinc site is mostly hydrophilic with extensive hydrogen-bonding. Phosphomannose binds within the cupin barrel at a site corresponding to the proposed oxalate binding site in OXDC.

Three cupins, isopenicillin *N*-synthase (IPNS) (*20*), homogentisate dioxygenase (HGDO) (*24*), and proline 3-hydroxylase (P3H) (*26*), are iron-dependent enzymes. All three enzymes are monocupins although HGDO contains a second partially formed cupin domain and displays a hexameric quaternary structure that is reminiscent of the OXDC structure. HGDO is unusual in that the cupin domain does not contain the metal site. Instead, the metal binding site is located near the interface between monomers within the partially formed cupin domain. The quaternary structure of P3H is dimeric while IPNS is monomeric. Like OXDC, each of the iron-containing cupins is oxygen dependent. dTDP-4-dehydrorhamnose 3,5-epimerase (*23*) is a dimeric monocupin with no reported metal binding site. The crystal structure showed that the substrate binding site is located within the barrel as is the case for the other enzymes of the cupin family. Likewise, the effector binding site of the

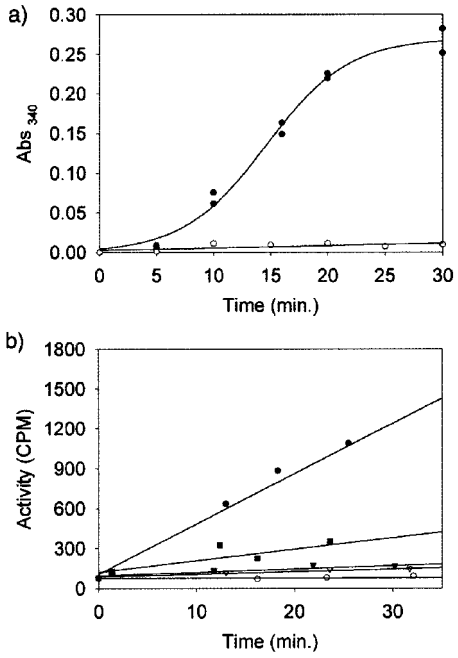

FIGURE 4: The catalytic activity of native and mutated OXDC. (a) Catalysis of formate production: Closed circles: native enzyme, Open circles: E333A mutant. (b) Catalysis of CO_2 production: Open circles: Native enzyme, Filled squares: E333A mutant; filled triangles: Y340F mutant; open triangle, R270E mutant; open circle: no enzyme.

transcription factor AraC (*22*) is located within the barrel. AraC functions as a dimer with no metal binding site. Although not all cupin family members have substrate binding sites and metal sites, these sites are structurally conserved when they are present.

The cupin fold of OXDC is structurally most similar to that of oxalate oxidase (*8*). Oxalate oxidase (OXO) is a hexameric monocupin with one manganese site per monomer. The sequence identity of OXO is about 15% compared to either domain I or domain II of OXDC. Like OXDC, OXO utilizes oxalate as substrate but catalyzes the oxidation of oxalate to CO_2 and H_2O_2 rather than a decarboxylation reaction. OXO is also reported to have a manganese superoxide dismutase activity (*8*). A three-dimensional alignment of the structure of OXO on the two individual domains I (Figure 5A) and II (Figure 5B) of OXDC resulted in a root-mean-square deviation (RMSD) for 150 Cα positions of 1.7 and 1.6 Å, respectively. Like OXDC, OXO has an extra loop region at the end of the β-barrel domain consisting of a short stretch of α-helices. These α-helices in OXO interlock in a claw-like fashion with the adjacent domain to form a planar hexameric structure that is similar to the seed storage protein trimers and the trimeric layer of OXDC. OXO utilizes its N-terminal region to form a dimeric unit that resembles the bicupin monomers of OXDC and the seed storage proteins.

Comparison of OXDC and OXO Manganese Binding Sites. The manganese binding sites in OXDC are similar to that of OXO as well as to each other. The manganese binding sites of OXO and of OXDC domains I and II have octahedral coordination with three conserved histidines and a conserved glutamic acid. Superpositions of each of the two manganese binding domains of OXDC to that of OXO are shown in Figure 5C,D. In addition to the four metal liganding residues, seven residues in the metal binding cavity are always hydrophobic. Given the overall structural similarity between OXDC and OXO, the similarity of the manganese binding sites and common substrate, it appears that only subtle changes are necessary to generate different biochemical activities. Additional factors other than the metal are necessary to differentiate between the oxidative decarboxylation and the nonredox decarboxylation. The most striking difference between the metal binding sites of the two proteins is the presence of Glu333 in domain II of OXDC while the equivalent residue in OXO is valine. The arginine residue in close proximity to the manganese binding site of each domain of OXDC is replaced by an asparigine residue in OXO. Other differences include Tyr340 in domain II, which is a proline residue in OXO, and hydrophobic residues in both domains I and II that are equivalent to Asn75 and Gln139 in OXO. It is possible that the absence of a proton donor in the active site of OXO prevents it from catalyzing the oxidative decarboxylation of oxalate to give formate.

Evidence of Internal Gene Duplication. OXDC has two structurally similar domains. Domain I consists of residues 51−223 and domain II consists of residues 224−378 plus the N-terminal residues 1 through 50 (Figure 6). The two domains were superimposed using the CCP4 program LSQKAB (*41*). The RMSD between the two domains for 200 Cα carbon atoms is 1.5 Å. Sequence comparison shows 27% identity between the two domains. The structural and sequence similarity suggests that OXDC is a product of gene duplication. The bicupin seed storage proteins also show evidence of gene duplication (*15*). Formation of the bicupin monomer in OXDC requires an additional crossover at the N-terminus that interlocks the two domains, while the monocupin OXO utilizes an N-terminal extension to form noncovalently linked dimers. After gene duplication, the N-terminal extension of OXDC may have evolved to serve as a covalent linker of cupin domains. The regions near the two metal binding centers in the two domains of OXDC are particularly well conserved. The main difference is that the hydrophobic residue Leu153 in domain I is replaced by the hydrophilic residue Glu333 in domain II. This substitution has catalytic implications as discussed below.

Intramolecular Channels. The hexameric structure of OXDC is characterized by three intramolecular channels. The most striking channel is along the 3-fold axis; however, this channel, which results from association of monomers, provides no apparent access to either metal binding site. Like the rest of the OXDC surface, the inside of this channel (Figure 2) is lined mostly with negatively charged residues. A similar channel is observed in the structures of the seed storage proteins and in OXO. The second channel is short and narrow and leads to the metal binding site of domain II (Figure 7A). The channel widens near the metal to include a hydrophobic pocket that might serve as the binding site for the product CO_2. There is one of these channels per monomer with three channels accessible from the top and three from the bottom of the hexamer as viewed in Figure 2A. The metal binding site of domain II is only accessible from the one side of the monomer. The third channel forms the entrance to the metal binding site of domain I (Figure 7B). The channels leading to the metal binding sites of domains I and II are related by an approximate 2-fold axis that is perpendicular to the plane in Figure 7C. Interestingly,

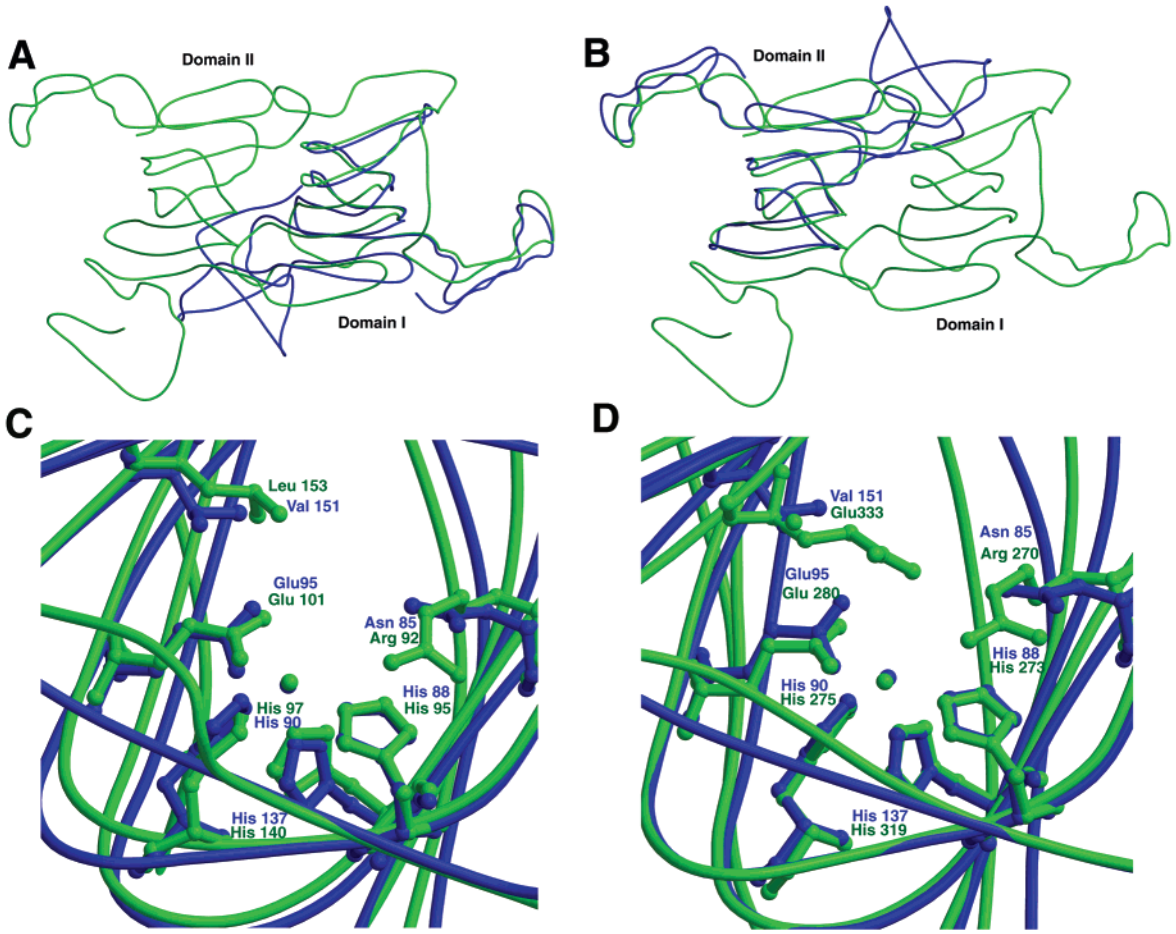

FIGURE 5: Superposition of the OXO monomer on the domains of OXDC. OXO is shown in blue. OXDC is shown in green. (A) Superposition of OXO on domain I of OXDC. (B) Superposition of OXO on domain II of OXDC. (C) Detail of the superimposed manganese binding sites of OXO and domain I of OXDC. (D) Detail of the superimposed manganese binding sites of OXO and domain II of OXDC. Metal liganding residues are labeled in green for OXDC and blue for OXO. The figure was prepared using MOLSCRIPT (*43*, *44*) and RASTER3D (*45*, *46*).

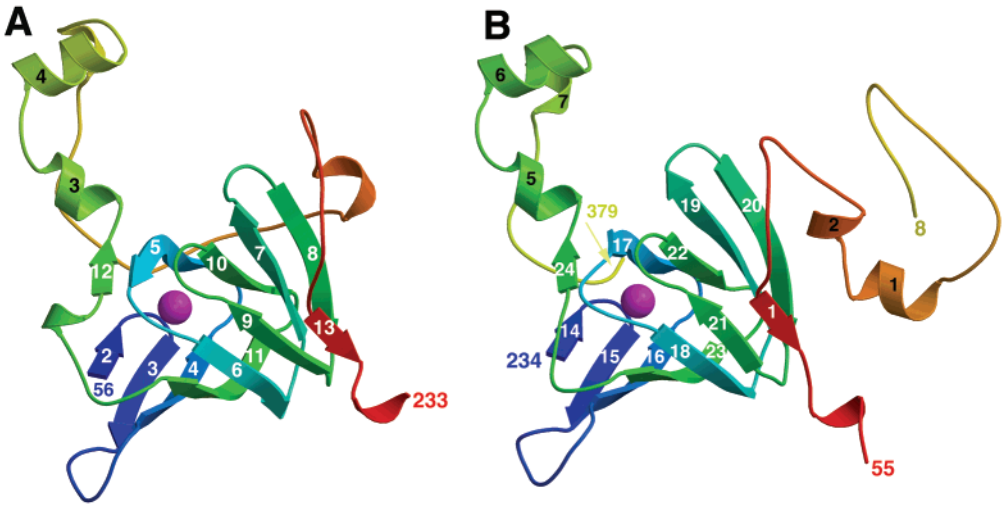

FIGURE 6: Structural similarity between the two domains of OXDC. Each domain is colored from blue at the N-terminus to red at the C-terminus. (A) Domain I includes residues 56−233. (B) Domain II includes residues 8−55 and 234−379. The figure was prepared using MOLSCRIPT (*43*, *44*) and RASTER3D (*45*, *46*).

the packing together of two trimeric layers to form the hexamer nearly occludes the openings of domain I for all six monomers. Consequently, the channel changes direction near the interface of the trimeric layers and exits near the equator of the hexamer. The entrance to the channel is lined by the hydrophilic residues Arg58, Glu60, Glu162, Glu198, and Tyr200 and preceded by a hydrophilic cavity at the surface of the hexamer. The channel is mostly hydrophobic near the metal binding site.

The hydrophilic cavity that serves as the entrance to the domain I channel is formed by three monomers. Loop 161−164 (SENS) from one monomer forms a well ordered 3_{10}

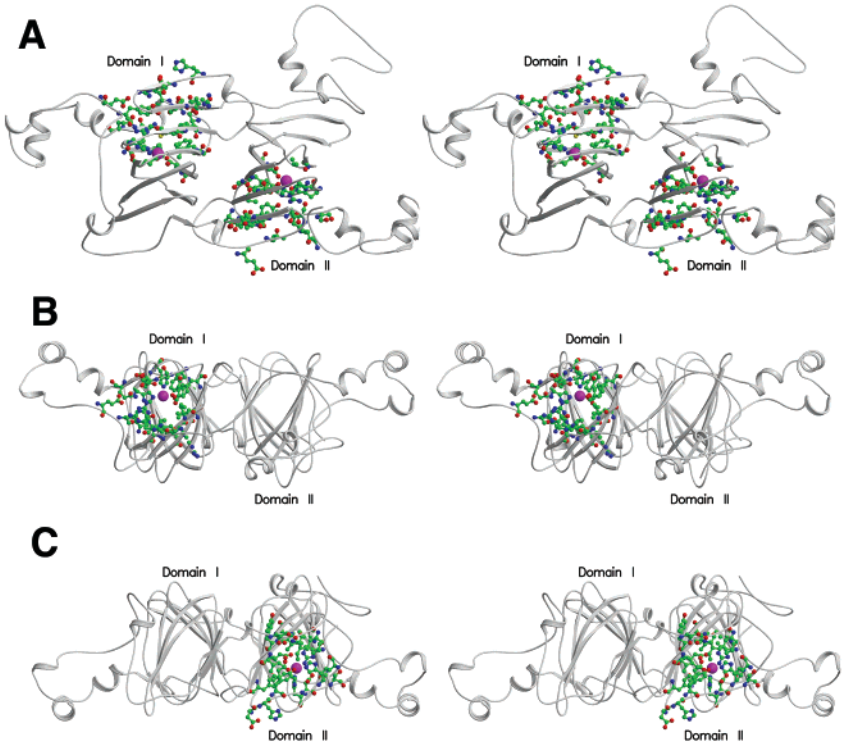

FIGURE 7: Channels in OXDC. (A) Stereoview looking into the channel that leads to the manganese site of domain II. (B) Stereoview looking into the channel that leads to the manganese site of domain I. (C) Stereoview showing the approximate 2-fold symmetry of the two metal binding site channels. Residues that line the channels are shown as ball-and-stick models. The figure was prepared using MOLSCRIPT (*43*, *44*) and RASTER3D (*45*, *46*).

helix. Glu162 is near Asp297 and His299 from the second monomer and Thr44 of the third monomer. The unknown metal binding site and the second formate site are also located near the channel entrance.

Identification of the Active Site. There are three metal centers on oxalate decarboxylase, a manganese center in domain I, a manganese center in domain II, and an unidentified metal binding site (modeled as Mg^{2+}) on the surface of the protein. The structural similarity between the domain I and domain II metal sites and the corresponding metal binding sites in the closely related oxalate oxidase suggests that these are the sites for catalysis. In addition, the surface metal ion is bound to the protein by only two ligands and is therefore likely to be at least partially lost during purification. Since addition of extra Mn(II) to the assay mixture did not result in enhanced activity, this site is unlikely to be the catalytic site and may result from high concentrations of ions that were added during purification and crystallization.

The presence of an enzymatic source for the acyl proton of formate is an important requirement for the catalysis of oxalate decarboxylation. In the domain II metal center, Glu333 appears to be suitably positioned for this function. The E333A mutant shows only 4% of the formate producing activity of the native enzyme (Figure 4a). Since there is no suitable proton donor close to the metal binding site in domain I, we conclude that the decarboxylation is occurring at the domain II site. The structure also suggests that Tyr340 may be the proton donor to the peroxide (see mechanistic proposal below) and that Arg270 may form an ion pair with the second carboxylate of the substrate. Our assignment of the active site is further supported by mutagenesis of these residues. The Y340F and R270E mutants show 8 and 5%, respectively, of the carbon dioxide producing activity of the native enzyme (Figure 4b). We were therefore surprised to find formate bound to the domain I site. Normally, the presence of bound substrate or product locates the active site, but in this case we believe that the reaction product may be binding to a regulatory site. It is also possible that domain I catalyzes a different enzymatic activity.

Scheme 1

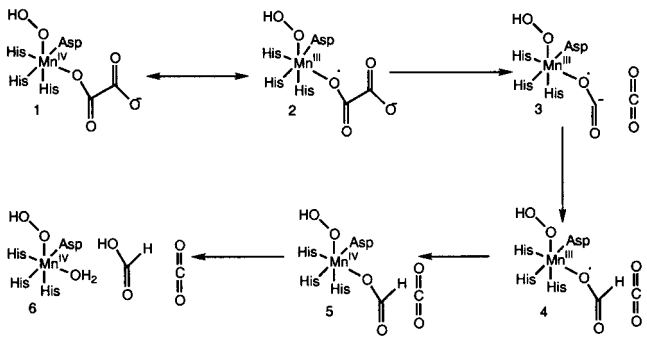

Proposed Catalytic Mechanism. The nonoxidative decarboxylation reaction catalyzed by OXDC presents a novel mechanistic problem because of the instability of the acyl carbanion. A radical based mechanism (*11*) and a mechanism involving an acyl peroxide intermediate (*13*) have been previously proposed. However, both mechanisms involve chemistry that is without precedent.

A mechanistic proposal for oxalate decarboxylase is outlined in Scheme 1. We suggest that the manganese(IV) hydroperoxide is the catalytically active form of the enzyme because of the oxygen requirement of the reaction (*13*). However, we cannot yet exclude the possibility that Mn(III), as the superoxide or generated by electron transfer from Tyr340 to **1**, is the catalytically important oxidation state.

Substrate binding, followed by the transfer of two electrons to the oxygen would give complex **1**, which can also be represented as **2**. Cleavage of the C−C bond of **2** would give **3**. This fragmentation is likely to be facile because the carbanion will be stabilized by the radical on the adjacent oxygen. Analogous 3-electron pi bonds have been used to explain the dramatic enhancement in the acidity of the alpha proton in amine radicals (*42*). Protonation of **3** at the carbanionic carbon, followed by inner sphere electron transfer from Mn(III) to the formyl radical and product dissociation, would complete the reaction.

The active site structure suggests that Tyr340 may be the proton donor to the peroxide, that Arg270 may form an ion pair with the second carboxylate of the substrate, and that the formate proton comes from Glu333. Consistent with these assignments, the activity of E333A, Y340F, and R270E mutants was reduced 25-, 13-, and 20-fold, respectively. Additional mutagenesis experiments and structural studies on OXDC complexes with substrate analogues are in progress to further clarify the mechanism of this interesting reaction.

ACKNOWLEDGMENT

We thank the Cornell High Energy Synchrotron Source for providing synchrotron beam time. We thank Dr. Joo-Heon Park and Ms. Nishat Shaikh for preparing the Y340F, R270E, and E333A mutations and Ms. Leslie Kinsland for assistance in the preparation of this manuscript.

REFERENCES

1. Banci, L., Bertini, I., Dal Pozzo, L., Del Conte, R., and Tien, M. (1998) *Biochemistry 37*, 9009−15.
2. Dunwell, J. M., Khuri, S., and Gane, P. J. (2000) *Microbiol. Mol. Biol. Rev. 64*, 153−79.
3. Kesarwani, M., Azam, M., Natarajan, K., Mehta, A., and Datta, A. (2000) *J. Biol. Chem. 275*, 7230−8.
4. Williams, H. E., and Wandzilak, T. R. (1989) *J. Urol. 141*, 742−9.
5. Kyriazakis, I., Anderson, D. H., and Duncan, A. J. (1998) *Br. J. Nutr. 79*, 55−62.
6. Keates, S. E., Tarlyn, N. M., Loewus, F. A., and Franceschi, V. R. (2000) *Phytochemistry 53*, 433−40.
7. Kostman, T. A., Tarlyn, N. M., Loewus, F. A., and Franceschi, V. R. (2001) *Plant Physiol. 125*, 634−40.
8. Woo, E. J., Dunwell, J. M., Goodenough, P. W., Marvier, A. C., and Pickersgill, R. W. (2000) *Nat. Struct. Biol. 7*, 1036−40.
9. Maloney, P. C. (1994) *Curr. Opin. Cell Biol. 6*, 571−82.
10. Lung, H. Y., Cornelius, J. G., and Peck, A. B. (1991) *Am. J. Kidney Dis. 17*, 381−5.
11. Emiliani, E., and Riera, B. (1968) *Biochim. Biophys. Acta 167*, 414−21.
12. Tanner, A., and Bornemann, S. (2000) *J. Bacteriol. 182*, 5271−3.
13. Tanner, A., Bowater, L., Fairhurst, S. A., and Bornemann, S. (2001) *J. Biol. Chem. 276*, 43627−34.
14. Ruiz Santamaria, J., Coll, R., and Fuentespina, E. (1993) *Clin. Biochem. 26*, 93−6.
15. Dunwell, J. M., and Gane, P. J. (1998) *J. Mol. Evol. 46*, 147−54.
16. Lawrence, M. C., Izard, T., Beuchat, M., Blagrove, R. J., and Colman, P. M. (1994) *J. Mol. Biol. 238*, 748−76.
17. Lawrence, M. C., Suzuki, E., Varghese, J. N., Davis, P. C., Van Donkelaar, A., Tulloch, P. A., and Colman, P. M. (1990) *EMBO J. 9*, 9−15.
18. Ko, T. P., Day, J., and McPherson, A. (2000) *Acta Crystallogr. D 56*, 411−20.
19. Ko, T. P., Ng, J. D., and McPherson, A. (1993) *Plant Physiol. 101*, 729−44.
20. Roach, P. L., Clifton, I. J., Fulop, V., Harlos, K., Barton, G. J., Hajdu, J., Andersson, I., Schofield, C. J., and Baldwin, J. E. (1995) *Nature 375*, 700−4.
21. Cleasby, A., Wonacott, A., Skarzynski, T., Hubbard, R. E., Davies, G. J., Proudfoot, A. E., Bernard, A. R., Payton, M. A., and Wells, T. N. (1996) *Nat. Struct. Biol. 3*, 470−9.
22. Soisson, S. M., MacDougall-Shackleton, B., Schleif, R., and Wolberger, C. (1997) *J. Mol. Biol. 273*, 226−37.
23. Giraud, M. F., Leonard, G. A., Field, R. A., Berlind, C., and Naismith, J. H. (2000) *Nat. Struct. Biol. 7*, 398−402.
24. Titus, G. P., Mueller, H. A., Burgner, J., Rodriguez De Cordoba, S., Penalva, M. A., and Timm, D. E. (2000) *Nat. Struct. Biol. 7*, 542−6.
25. Borgstahl, G. E., Pokross, M., Chehab, R., Sekher, A., and Snell, E. H. (2000) *J. Mol. Biol. 296*, 951−9.
26. Clifton, I. J., Hsueh, L. C., Baldwin, J. E., Harlos, K., and Schofield, C. J. (2001) *Eur. J. Biochem. 268*, 6625−6636.
27. Adachi, M., Takenaka, Y., Gidamis, A. B., Mikami, B., and Utsumi, S. (2001) *J. Mol. Biol. 305*, 291−305.
28. Clissold, P. M., and Ponting, C. P. (2001) *Trends Biochem. Sci. 26*, 7−9.
29. Bradford, M. M. (1976) *Anal. Biochem. 72*, 248−54.
30. Leslie, A. G. W. (1997) MOSFLM Version 5.40, *MRC Laboratory of Molecular Biology*, Cambridge, UK.
31. Evans, P. R. (1993) SCALA Version 3.3, *MRC Laboratory of Molecular Biology*, Cambridge, UK.
32. Miller, R., DeTitta, G. T., Jones, R., Langs, D. A., Weeks, C. M., and Hauptman, H. A. (1993) *Science 259*, 1430−3.
33. Smith, G. D., Nagar, B., Rini, J. M., Hauptman, H. A., and Blessing, R. H. (1998) *Acta Crystallogr. D 54*, 799−804.
34. Miller, R., Gallo, S. M., Khalak, H. G., and Weeks, C. M. (1994) *J. Appl. Crystallogr. 27*, 613−621.
35. Otwinowski, Z. (1991) in *Proceedings of the CCP4 Study Weekend: Isomorphous Replacement and Anomalous Scattering* (Wolf, W., Evans, P. R., and Leslie, A. G. W., Eds.) pp 80−88, SERC Proceedings, Daresbury Laboratories, Worthington, UK.
36. Cowtan, K. (1994) *Joint CCP4 and ESF-EACBM Newsletter on Protein Crystallography* Vol. 31, pp 34−38, Collaborative Computation Project No. 4, Daresbury, UK.
37. Jones, T. A., Zou, J.-Y., Cowan, S. W., and Kjeldgaard, M. (1991) *Acta Crystallogr. A 47*, 110−119.
38. Brünger, A. T., Adams, P. D., Clore, G. M., DeLano, W. L., Gros, P., Grosse-Kunstleve, R. W., Jiang, J. S., Kuszewski, J., Nilges, M., Pannu, N. S., Read, R. J., Rice, L. M., Simonson, T., and Warren, G. L. (1998) *Acta Crystallogr. D 54*, 905−21.
39. Harding, M. M. (1999) *Acta Crystallogr. D 55*, 1432−43.
40. Holm, L., and Sander, C. (1994) *Proteins 19*, 165−73.
41. Kabsch, W. (1976) *Acta Crystallogr. A 32*, 922−923.
42. Jonsson, M., Wayner, D. D. M., and Lusztyk, J. (1996) *J. Phys. Chem. 100*, 17539−17543.
43. Esnouf, R. M. (1997) *J. Mol. Graphics 15*, 132−134.
44. Kraulis, P. J. (1991) *J. Appl. Crystallogr. 24*, 946−950.
45. Merritt, E. A., and Bacon, D. J. (1997) *Methods Enzymol. 277*, 505−524.
46. Merritt, E. A., and Murphy, M. E. P. (1994) *Acta Crystallogr. D 50*, 869−873.

BI0200965